

1 **Thermal state and evolving geodynamic regimes of the**
2 **Meso- to Neoproterozoic North China Craton**

3
4 Guozheng Sun¹, Shuwen Liu^{1, *}, Peter A. Cawood^{2, *}, Ming Tang¹, Jeroen van Hunen³,
5 Lei Gao¹, Yalu Hu¹, Fangyang Hu^{4,5}

6
7
8 ¹*Key Laboratory of Orogenic Belts and Crustal Evolution, Ministry of Education,*
9 *School of Earth and Space Sciences, Peking University, Beijing 100871, PR China*

10 ²*School of Earth, Atmosphere and Environment, Monash University, Melbourne, VIC*
11 *3800, Australia*

12 ³*Department of Earth Sciences, Durham University, Durham DH1 3LE, UK*

13 ⁴*State Key Laboratory of Lithospheric Evolution, Institute of Geology and Geophysics,*
14 *Chinese Academy of Sciences, Beijing 100029, PR China*

15 ⁵*Department of Geosciences, University of Arizona, Tucson, AZ 85721, USA*

16
17 Manuscript for *Nature communications*

18
19 ***Corresponding authors**

20 Shuwen Liu (swliu@pku.edu.cn)

21 Peter A. Cawood (peter.cawood@monash.edu)

23 Constraining the thickness and geothermal gradient of Archean continental crust are
24 crucial to understanding geodynamic regimes of the early Earth. Archean crust-sourced
25 tonalitic–trondhjemitic–granodioritic gneisses are ideal lithologies for reconstructing
26 the thermal state of early continental crust. Integrating experimental results with
27 petrochemical data from the Eastern Block of the North China Craton allows us to
28 establish temporal–spatial variations in thickness, geothermal gradient and basal heat
29 flow across the block, which we relate to cooling mantle potential temperature and
30 resultant geodynamical regime change from plume dominated in the late Mesoarchean
31 (~2.9 Ga) to plate tectonics with hot subduction in the early to late Neoproterozoic (~2.7–
32 2.5 Ga). The initiation of plate tectonics might have played an important role in the
33 rapid cooling of the mantle, and thickening and strengthening of the lithosphere, which
34 in turn prompted stabilization of the cratonic lithosphere at the end of Archean.

35 The Archean Earth (4.0–2.5 Ga) was characterized by higher upper-mantle potential
36 temperatures (T_p), higher mantle heat flow, and significantly less differentiated
37 lithosphere than the present day^{1–4}. Numerical models using these inferred Archean
38 conditions have suggested a geodynamical evolution from “no-subduction” to “pre-
39 subduction” and then to “modern subduction” regimes with the progressive decrease of
40 the mantle potential temperature^{5–7}. However, the timing and conditions under which
41 the Earth transitioned to a plate tectonic regime are controversial due to, and dependent
42 on, poorly constrained estimates for the transition between different thermal states^{8–13}.
43 Crustal thickness, Moho temperature and heat flow are direct reflections of the thermal
44 conditions of Earth’s lithosphere, and profoundly influence lithospheric rheology and
45 tectonics. Therefore, constraining these parameters will provide important new insight
46 in Archean geodynamic^{14–17}.

47 Archean cratons are dominated by metamorphic basement terranes composed of
48 high-grade tonalite–trondhjemite–granodiorite (TTG) gneisses and granite-greenstone
49 belts. The former constituting some 70 % of the crustal volume and thus, their formation
50 plays a crucial role in the unravelling the evolution of the ancient continental crust¹⁸.
51 Recent investigations suggest that the magmatic precursors of the TTG gneisses may
52 be derived from (1) fractionation of primary basaltic or dioritic magmas (namely,
53 “crystal mush model”)^{19–21}; (2) partial melting of hydrated mafic rocks at the base of
54 the Earth’s crust^{22,23}; or, (3) partial melting of fluid fluxed mantle (namely, “slab
55 melting model”)^{24–26}. The most prominent features of TTG melts derived from partial
56 melting of thickened lower crust are lower MgO content (generally less than 2.0 wt.%)

57 and transition elements of Cr, Ni, Co and V concentrations with Mg# values (Mg# =
58 $\text{Mg}^{2+}/(\text{Mg}^{2+}+\text{Total Fe}^{2+}) \times 100$) lower than 45 based on the results of experimental
59 petrology²⁷. In contrast, the TTG melts formed by the melting of fluid fluxed mantle
60 and the crystallization of basaltic or dioritic magmas usually show higher MgO (> 2.0
61 wt.%) and transition element contents with Mg# values higher than 45^{28,29}. The pressure
62 (P) conditions of crustal-derived TTG gneisses may be used to estimate the minimum
63 crustal thickness, and the temperature (T) conditions can represent the lower limit of
64 Moho surface temperature. Following the geothermal models proposed by Chapman³⁰,
65 we can quantitative calculate the Moho geothermal gradient and basal heat flow (q_B)
66 assuming a steady-state conductive geotherm³¹. Therefore, the Archean crust-sourced
67 TTG gneisses are ideal lithologies for reconstructing the thermal state of early
68 continental crust.

69 In this contribution, we compile the geochemical data for multiple episodes of Meso-
70 to Neoarchean (~2.9, ~2.7 and ~2.5 Ga) TTG gneisses from the Eastern Block of the
71 North China Craton (NCC) (Supplementary Fig. 1), and try to quantify the P–T
72 conditions of the TTG magma, using the proportion of garnet in residual phases from
73 partial melting process, Sr/Y ratios in the TTG melts, and thermodynamic and trace
74 element modelling. This allows the crustal thickness, Moho geothermal gradient and
75 basal heat flow (q_B) in the studied periods of the Archean to be calculated. On the basis
76 of the newly obtained crucial parameters, we propose a systematic evolution of Archean
77 geodynamic regimes to explain the formation and evolution of early continental
78 lithosphere.

79 **Results**

80 **Data selection.** This study is based on a dataset of 304 analyses (including both
81 previously published and our latest data) of ca. 2.9 to 2.5 Ga TTG gneisses from the
82 Eastern Block of the NCC. These TTG gneiss samples were collected from Anhui,
83 Zhongtiao, Dengfeng-Taihua, East Hebei-West Liaoning, South Jilin-North Liaoning,
84 West Liaoning, and Jiaodong terranes in the Eastern Block of the North China Craton
85 (Supplementary Fig. 1). For a detailed description of each terrane, see Supplementary
86 Figs. 2–9. New samples were analyzed for major and trace element by X-ray
87 Fluorescence (XRF) and Inductively Coupled Plasma–Mass Spectrometry (ICP–MS)
88 methods at the Key Laboratory of Orogenic Belts and Crustal Evolution, Ministry of
89 Education, School of Earth and Space Sciences, Peking University.

90 Archean TTG gneisses in the study area can be roughly divided into two groups based
91 on the MgO versus SiO₂ diagram (Fig. 1a): (1) low-magnesium TTGs, and (2) high-
92 magnesium TTGs. Both groups of TTG samples are characterized by high SiO₂ (> 60
93 wt.%) and Al₂O₃ (> 14 wt.%) contents but low K₂O/Na₂O ratios (< 0.6), which all
94 satisfy the classical definition of Archean TTGs²². These samples mainly plot in the
95 sub-alkaline quartz monzonite, granodiorite and granite fields in the TAS diagram (Fig.
96 1b), the tonalite and trondhjemite fields in the An–Ab–Or diagram (Fig. 1c), and are
97 assigned to low- to medium-K calc-alkaline rock series (Fig. 1d). The high-magnesium
98 TTGs show relatively high MgO contents (0.87–4.20 wt.%) and Mg# values (43–62),
99 falling into the high-silica adakite field (Fig. 1a)¹⁸. These features, together with their
100 relatively high contents of transitional elements (V, Cr, Ni, and Co), indicate that these

101 TTG melts formed by melt–mantle interactions²⁸, and thereby cannot provide effective
102 information for crustal thermal state. By contrast, the relatively low MgO (0.10–3.05
103 wt.%), Ni, Cr contents and Mg# values (18–48) of low-magnesium TTGs are indicative
104 of derivation of the magmatic precursors from melting of the lower portion of a thick
105 mafic crust (Fig. 1a)^{27,32}. Thus, the formation P–T conditions of low-magnesium TTGs
106 may effectively represent the thermal state of early continental crust. Furthermore, only
107 the samples with precise zircon magmatic ages can be used to constrain the geodynamic
108 regimes of the early Earth. After carefully screening, only 105 analyses of low-
109 magnesium TTGs meet the above criteria and we create data subsets by grouping
110 individual analyses with similar ages (Supplementary Tables 1–3).

111 **Magma source characteristics.** The zircon Hf isotopic compositions of the dated
112 low-magnesium TTG gneiss samples distribute mainly between CHUR (chondrite
113 uniform reservoir) and DM (depleted mantle) lines and fall within the same crustal
114 evolution range (Fig. 2a; Supplementary Table 4). These relationships imply that the
115 TTG gneisses with different ages were likely derived from juvenile crustal sources with
116 similar chemical composition, namely, the lower crust of the NCC. In the Mg# versus
117 SiO_2 and $\text{Al}_2\text{O}_3/(\text{FeO}_{\text{tot}}+\text{MgO})-3\times\text{CaO}-5\times(\text{K}_2\text{O}/\text{Na}_2\text{O})$ source discriminate diagrams,
118 almost all the gneisses fall into the melt range of amphibolite and eclogite, and plot into
119 the field of melts derived from low-K mafic rocks (Fig. 2b, c)³³. This further confirms
120 that the Archean metamorphic low-K basalts may be the most appropriate source rocks
121 for these low-Mg TTG gneisses. Considering these isotopic and geochemical
122 characteristics, we choose the Archean ‘arc-like’ basalts as the starting materials with

123 reference to the composition of enriched tholeiitic basalts^{22,34}. Subsequently, a batch
124 partial melting model is applied to explore the garnet proportions in the residual mineral
125 assemblage for the Meso- to Neoproterozoic TTG gneisses in the Eastern Block of the NCC.
126 Geochemical modelling reveal that the late Mesoproterozoic (~2.9 Ga) TTG gneisses
127 possess ~10 % (Anhui), ~20 % (Jiaodong) and ~10 % (East Hebei) garnet in the residual
128 phase from partial melting of the mafic sources (Fig. 2d), the early Neoproterozoic (~2.7
129 Ga) TTG gneisses have ~25 % (West Shandong), ~30 % (North Liaoning-South Jilin
130 and Jiaodong) and 35 % (Zhongtiao) garnet in the residue (Fig. 2e), and the late
131 Neoproterozoic (~2.5 Ga) TTG gneisses contain ~10 % (West Shandong and Jiaodong),
132 15 % (North Liaoning-South Jilin), 20 % (Zhongtiao), 25 % (Dengfeng-Taihua) and
133 25 % (East Hebei-West Liaoning) garnet in the residue (Fig. 2f). Therefore, the magmas
134 of TTG gneiss samples collected from different formation times and localities were
135 generated by the partial melting of low-K mafic juvenile crust materials at different
136 depths.

137 **Estimation of the thermal state for North China Craton.** Thermodynamic and
138 trace element modelling was performed using the median composition of Archean ‘arc-
139 like’ basalts with ~1.5 wt.% water to better define the P–T conditions of the primary
140 magma (Fig. 3). The pressure ranges of the magma generation for different age TTG
141 gneisses were used to estimate minimum thickness of the North China continental crust
142 at the time of gneiss formation, indicating crustal thickness and Moho geothermal
143 gradient evolved from 32–41 km and 18.2–22.8 °C/km, in the Mesoproterozoic, to 41–54
144 km and 9.9–16.8 °C/km in the early Neoproterozoic and 35–56 km thick crust and 8.7–18.0

145 °C/km Moho gradient at the end of the Neoproterozoic (Table 1). Based on the newly
146 obtained crustal thickness, the temperature at the bottom of continental crust (T_B), and
147 the classical geotherm models proposed by Chapman³⁰, we reconstruct the Archean
148 continental geotherm assuming a steady-state conductive geotherm (Fig. 4)³¹. The
149 calculated results yield the Moho geothermal gradients and basal heat flows of 18.2–
150 22.8 °C/km and 47–59 mW/m² for ~2.9 Ga TTG gneisses, 9.9–16.8 °C/km and 26–44
151 mW/m² for ~2.7 Ga TTG gneisses, and 8.7–18.0 °C/km and 23–47 mW/m² for ~2.5 Ga
152 TTG gneisses (Table 1).

153

154 Discussion

155 **Tempo-spatial variations in the thermal state of Meso- to Neoproterozoic**
156 **continental crust.** The trace element and thermodynamic modelling results reveal that
157 the paleo-crustal thickness has changed significantly through time in the Eastern Block
158 of the NCC (Fig. 5a). Crustal thickness increased rapidly from ~36 to ~48 km from ~2.9
159 to ~2.7 Ga, then remained mostly constant during ~2.7 to ~2.5 Ga, with the exception
160 of the North Liaoning-South Jilin, Jiaodong and West Shandong terranes, where the
161 crustal thickness decreased about 10 km (Fig. 5a). Archean continental geotherm
162 modelling suggests that the Moho geothermal gradient and basal heat flow value exhibit
163 consistent trends and decreased dramatically from ~2.9 to ~2.7 Ga and then remain
164 unchanged from ~2.7 to ~2.5 Ga (Figs. 4 and 5a). Contour maps of crustal thickness
165 and Moho geothermal gradients of the Eastern Block of the NCC show that in the early

166 Neoproterozoic (~2.7 Ga), the North Liaoning-South Jilin and West Shandong regions have
167 relatively thick crust but low Moho geothermal gradients, whereas the Jiaodong and
168 Zhongtiao terranes exhibit relatively thin crust but high Moho geothermal gradients
169 (Fig. 6a, c). By the late Neoproterozoic (~2.6–2.5 Ga), the crustal thickness and Moho
170 geothermal gradient display obvious spatial zonation, for instance, the western margin
171 of the Eastern Block (East Hebei-West Liaoning, Dengfeng-Taihua, Zhongtiao) shows
172 relatively thickened crust and low Moho geothermal gradients, but the eastern margin
173 of the Eastern Block (North Liaoning-South Jilin, Jiaodong, West Shandong) exhibits
174 relatively thin crust and high Moho geothermal gradients (Fig. 6b, d).

175 **Evolution of Archean geodynamic regimes of the NCC.** The operation, scale, and
176 style of tectonic regimes in the formation and evolution of the Archean continental crust
177 are mainly dependent on the mantle temperature as shown by thermomechanical
178 numerical experiments^{5–7}. Nevertheless, such models do not constrain a timeframe for
179 such elevated mantle temperatures. This study enables us to link those temperatures to
180 geological time. In the Archean continental geotherm model, the variation of basal heat
181 flow (q_B) is mostly attributed to the mantle potential temperatures and the depth of
182 thermal boundary (lithospheric thickness) (Fig. 4). Keller and Schoene³⁵ proposed that
183 the above two variables have a direct causal relationship in the lithospheric evolution
184 process prior to 2.5 Ga. A decrease in mantle potential temperature may be linked to the
185 emergence of thick lithosphere in the Archean. Combining our constraints on the Meso-
186 to Neoproterozoic crustal thicknesses and thermal states with previous numerical
187 experiments, petrological and structural studies, a systematic three-stage evolution of

188 the Archean geodynamic regime has been revealed in the Eastern Block of the NCC.

189 (1) The Eastern Block exhibits a relative thin crustal thickness of 32 to 41 km, high
190 Moho geothermal of 18.2 to 22.8 °C/km (Fig. 5a, b; Table 1), and high basal heat flow
191 values of $q_B = 47\text{--}59$ mW/m² during ~2.9–2.8 Ga, reflecting the higher mantle potential
192 temperature and the thinner lithosphere thickness relative to younger time periods (Figs.
193 4 and 5c). Hot-mantle potential temperatures in the late Mesoarchean and the
194 development of coeval komatiites and komatiitic basalts in the Eastern Block
195 presumably favor the mantle plume regime^{3,36}. Coincidentally, Bao et al.³⁷ also propose
196 a pre-subduction buckling convergence model to explain the petrogenesis of the
197 compositionally diverse Mesoarchean granitoids in the Anshan-Benxi area in the
198 eastern part of the NCC.

199 (2) The crustal thickness began to increase rapidly from the late Mesoarchean (~2.8
200 Ga) and reached its maximum thickness of ~41–54 km by the early Neoproterozoic (~2.7
201 Ga), while the Moho geothermal gradient decreased from ~18.2–22.8 to ~9.9–
202 16.8 °C/km (Fig. 5a, b; Table 1). During this crustal thickening period, the basal heat
203 flow decrease significantly reflecting rapid cooling of convecting mantle and/or
204 thickening of the lithosphere (Figs. 4 and 5c). On the other hand, the mantle cooling
205 also promote lithosphere strengthening. Integrated with petrological and structural data
206 for a corresponding change through this interval from komatiite to calc-alkaline
207 volcanic rock, and a changing structural style from extension to compression²⁶, these
208 newly obtained data indicate that plate tectonics were already a dominant geodynamic
209 mechanism in the Neoproterozoic. However, the style of Archean plate tectonics (for

210 example, subduction rate and subducted angle of oceanic slab) in North China may have
211 been different from that of modern day cold plate tectonics due to its slightly higher
212 mantle temperature on the basis of the thermomechanical numerical modeling results,
213 and is often referred to as “hot subduction”^{38,39}. Therefore, the Mesoproterozoic-
214 Neoproterozoic transition (~2.8 Ga) is considered as a critical period for the transformation
215 of the crust-mantle dynamic regimes, in which a hot subduction regime (lateral plate
216 movement) began to play an important role in the crustal growth and evolution in the
217 Eastern Block of the NCC.

218 (3) Crustal stabilization period is marked by various crustal thickness of 54 to 35 km,
219 Moho geothermal gradient of 8.7 to 18.0 °C/km, and basal heat flow of 23–47 mW/m²
220 during ~2.7–2.5 Ga. These values decrease slightly from those of the preceding period
221 suggesting a likely continuity of the tectonic regime dominated by hot subduction (Figs.
222 4 and 5). In the thermomechanical numerical model of plate tectonics on the early Earth,
223 as a subduction zone matures, mantle potential temperature continues to decrease
224 whereas the strength of lithospheric plates gradually increase, resulting in the formation
225 of larger-scale tectonic belts that resemble those produced by modern plate
226 subduction^{40,41}. By the early to late Neoproterozoic, many lines of evidence indicate that
227 the Eastern Block of the NCC underwent an orogenic cycle of subduction, collision and
228 delamination events: (1) the thermal state of continental crust is spatially zoned (Fig.
229 6b, d; Table 1), which are similar to the thermal structure of present-day continental
230 subduction zones such as North Cordilleran and Central Andean⁴²; (2) marked spatial
231 zoning of metamorphic volcanic rocks, TTG gneisses and K-rich granitoids occurs

232 along the northwestern side of the Eastern Block^{40,43,44}; and (3) *in-situ* zircon O isotopes
233 for Neoproterozoic metavolcanic rocks from the Dengfeng Complex indicates that altered
234 oceanic crust was involved in the mantle source region, requiring recycling of oceanic
235 crust into the mantle, presumably at a subduction zone⁴⁵.

236 At the end of Archean (~2.5 Ga), a large amount of K-rich granitoids in the NCC
237 appeared along with a corresponding reduction in the proportion of TTG gneisses⁴⁶.
238 Post-Archean high-Mg-K granitoids throughout the Eastern Block show similar
239 geochemical signatures to Archean sanukitoids, and their magmas were derived from
240 mantle metasomatism by fluids as well as melts from subducting slab and sediments in
241 late-orogenic settings^{44,47,48}. These geological observations and crust-mantle
242 interactions, together with relatively low mantle potential temperature and thick
243 lithosphere, imply the development of rigid lithosphere and the final cratonization of
244 the Eastern Block during the terminal Archean. Similar features have been noted in
245 other cratons towards the end of the Archean corresponding with their stabilization and
246 inferred to mark a global transition to a dominant plate tectonic regime¹².

247 **Implications for global-scale ancient cratons.** Understanding the changes of
248 Earth's thermal state is essential to determining the geodynamic evolution of the early
249 Earth. Moyen (2011)⁴⁹ summarized the 1477 samples of Archean (~3.5–2.5 Ga) TTG
250 gneisses from global ancient cratons and classified them into three different categories
251 (high-pressure, medium-pressure and low-pressure subgroups) based on their
252 geochemical indicators (i.e., Sr contents, Sr/Y and La/Yb ratios). Petrogenetic studies
253 revealed that most medium-pressure (MP) and low-pressure (LP) TTGs were originated

254 from thickened mafic lower crust, whereas most high-pressure (HP) TTGs were derived
255 from subducted slab^{22,34,49}. Therefore, only the MP and LP TTGs are suitable for
256 estimating the thermal state of early continental crust (698 samples) by our method. The
257 estimated results indicate that the crustal thicknesses, Moho geothermal gradients and
258 basal heat flow values are 40–44 km, 17.6–22.0 °C/km and 53–66 mW/m² for MP TTGs,
259 and 32–36 km, 22.1–27.5 °C/km and 66–83 mW/m² for LP TTGs, respectively. It's
260 noteworthy that our estimated Archean continental crust had a similar crustal thickness
261 to the present-day craton⁵⁰, which is a big challenge to conventional wisdom with
262 respect to the Archean crustal thickness^{9,51}. Meanwhile, the new results also provide an
263 effective constraint on the thermal state of the Archean continental crust, which is
264 significantly higher than it is present-day counterparts⁵². Collectively, the crustal
265 thickness and its thermal state are crucial to our understanding of the geodynamic
266 regime of the early Earth.

267

268 **Methods**

269 **Samples.** TTG gneisses are the dominant geological signatures in the Archean
270 basement blocks of the NCC. [Supplementary Fig. 1](#) shows the general spatial and
271 temporal distribution of Meso- to Neoarchean TTG gneisses, and detailed zircon age
272 data and sampling locations are summarized in [Supplementary Table 1](#). The magmatic
273 crystallization ages of TTG gneisses are almost continuous from 3.0 to 2.5 Ga, with
274 three peaks occurring at ~2.91, ~2.72 and ~2.53 Ga, with the youngest defining the

275 maximum peak. The ~ 2.9 Ga TTG gneisses are sporadically distributed in Jiaodong,
276 Huoqiu and Eastern Hebei terranes, and ~ 2.7 Ga ages TTG gneisses concentrate more
277 in the North Liaoning-South Jilin, Jiaodong, Western Shandong, Dengfeng-Taihua,
278 Zhongtiao and Fuping-Hengshan terranes, while the ~ 2.5 Ga data are distributed
279 throughout the entire Eastern Block of the NCC. All the TTG gneisses, irrespective of
280 age exhibit similar petrographic characteristics, making the different age groups
281 difficult to distinguish in the field. A detailed outline of the geological background of
282 each terrane is given in the [Supplementary Information](#).

283 **Selection of mafic source rocks of the TTG magmatism.** The potential mafic
284 source rocks for Archean TTG magmas mainly comprise mid-ocean ridge basalts
285 (MORBs), oceanic plateau basalts (OPBs), island arc basalts (IABs) and Archean ‘arc-
286 like’ basalts according to their tectonic setting³⁴. The Archean ‘arc-like’ basalts are
287 chiefly composed of moderately enriched tholeiitic basalts, which have similar
288 lithological assemblages and trace element compositions with those found in modern
289 oceanic arcs. Here, we compiled the average composition of potential mafic source
290 rocks for Archean TTG magmatism from the GEOROC ([http://georoc.mpch-](http://georoc.mpch-mainz.gwdg.de/georoc/)
291 [mainz.gwdg.de/georoc/](http://georoc.mpch-mainz.gwdg.de/georoc/)) and PetDB (www.earthchem.org/petdb) databases
292 ([Supplementary Table 5](#)). Among them, the MORBs and OPBs are too depleted in large
293 ion lithophile elements (LILEs) to produce TTG gneisses, whereas the melts from the
294 partial melting of IABs tend to be potassium-rich granitoids. Only the Archean ‘arc-
295 like’ basalts are suitable to be the source rocks of the TTG gneisses ([Supplementary Fig.](#)
296 [12](#)). Consequently, we choose the Archean ‘arc-like’ basalts as the mafic source rocks

297 of the TTG magmatism in the thermodynamic and trace element modelling.

298 **Determination of source water content [X(H₂O)].** CIPW (Cross, Iddings, Pirsson,
299 Washington) standard mineral calculation results show that the corresponding mineral
300 assemblages and their proportions of the Archean ‘arc-like’ basalts are as follows:
301 quartz, 3.04 wt.%; orthoclase, 1.59 wt.%; albite, 17.74 wt.%; anorthite, 29.94 wt.%;
302 diopside, 16.35 wt.%; hypersthene, 27.62 wt.%; magnetite, 1.85 wt.%; ilmenite, 1.65
303 wt.%; and, apatite, 0.22 wt.%. Note that the CIPW calculation only yields the mass
304 fraction of various standard minerals in the magmatic rock, which simplifies many
305 details (for example, all the standard minerals are anhydrous, leaving out the hydrous
306 minerals biotite and amphibole). The melting processes of metabasalts are dominantly
307 controlled by amphibole dehydration melting reactions at fluid-absent conditions⁵³.
308 Assuming that all these mafic minerals (diopside and hypersthene) in the standard
309 minerals are amphibole (H₂O content in standard amphibole is known to be ~3.5
310 wt.%)⁵⁴, the water content in Archean ‘arc-like’ basalts is less than ~1.54 wt.%, and the
311 average LOI (loss on ignition) of the Archean ‘arc-like’ basalts is ~1.69 wt.%, which is
312 basically consistent with the conversional results on the basis of the CIPW standard
313 mineral calculation. Therefore, the ~1.5 wt.% is taken as the water content [X(H₂O)] of
314 Archean mafic protolith in the lower crust.

315 **Thermodynamic modelling of primary magma.** Thermodynamic modelling was
316 performed using the median composition of Archean ‘arc-like’ basalts to better define
317 the P–T conditions of the primary magma, following a Gibbs free energy minimization
318 approach using the software Perple_X (version 6.7.6). Due to the low content of bulk

319 P₂O₅ and the lack of associated phases (i.e., apatite) in the rock, we choose a system
320 Na₂O-CaO-K₂O-FeO-MgO-Al₂O₃-SiO₂-H₂O-TiO₂-O₂ (NCKFMASHTO) for the
321 thermodynamic modelling, and use the thermodynamic database from Holland and
322 Powell⁵⁵ revised in 2002 (hp02ver.dat), together with the solution models of Melt(G)
323 for TTG melt, cAmph(G) for amphibole, and Augite(G) for clinopyroxene from Green
324 et al.⁵⁶, Gt(W) for garnet, Opx(W) for orthopyroxene, Ilm(WPH) for ilmenite, Chl(W)
325 for chlorite, and Mica(W) for mica from White et al.⁵⁷, Bi(HP) for biotite from Holland
326 and Powell⁵⁵, Fsp(C1) for plagioclase from Holland and Powell⁵⁸, and Ep (HP11) for
327 epidote from Holland and Powell⁵⁹. The quartz, rutile, titanite, and water were
328 considered as pure phases. The calculation was performed with 1.5 wt.% water,
329 corresponding to the dehydrated melting of metamorphosed basalt.

330 **Batch partial melting modelling.** Since the thermodynamic modelling yields the
331 weight percentages of melts and equilibrium mineral assemblages, we can further
332 calculate the trace element composition of the TTG melts through trace element
333 modelling. Shaw⁶⁰ proposed the classical equation of batch partial melting:

334
$$C_{\text{melt}}/C_{\text{source}} = 1/[D + F*(1-D)]$$

335 Where C_{source} and C_{melt} represent the trace element concentration of the source rock
336 and the resultant melt, respectively; D is the bulk partition coefficient, and F is the
337 degree of partial melting (namely, the mass fraction of melt). The median composition
338 of the Archean ‘arc-like’ basalts were used as the C_{source}, and the results (C_{melt}) were
339 compared with the median composition of TTG gneisses with different ages of ~2.9 to
340 ~2.5 Ga. The partition coefficient of minerals used in the geochemical modelling are

341 from <https://earthref.org/GERM/KDD/> ([Supplementary Table 6](#)).

342 **Geothermal models.** If the layer has thickness Δz , then the temperature at, and heat
343 flow through, the bottom of the layer (T_B , q_B) can be expressed in terms of the
344 temperature and heat flow at the top of the layer (T_T , q_T) and properties (A, k) of the
345 layer³⁰.

$$346 \quad T_B = T_T + \frac{q_T}{k} \Delta z - \frac{A \Delta z^2}{2k} \quad (1)$$

$$347 \quad q_B = q_T - A \Delta z \quad (2)$$

348 Equations (1) and (2) are applied to successive layers, resetting T_T and q_T at the top of
349 each new layer with the values T_B and q_B solved for the bottom of the previous layer.

350 Where A is volumetric heat production (W m^{-3}) and k is thermal conductivity (W m^{-1}
351 K^{-1}). In practice, heat production and thermal conductivity are described by piecewise
352 continuous functions and the computations are carried out with a 0.1 km depth
353 increment. Following Tang et al.⁶¹, the volumetric heat production in the crust is:

$$354 \quad A_j = \sum_j F_j \rho \sum_i H^i C_j^i e^{-\lambda^i t} \quad (3)$$

355 where $i = {}^{40}\text{K}$, ${}^{232}\text{Th}$, ${}^{235}\text{U}$ and ${}^{238}\text{U}$, j indicates mafic and felsic crust, F is volumetric
356 proportion, ρ is the density (2800 kg m^{-3}), λ^i is the decay constant (yr^{-1}), t is time before
357 present (yr), H^i is heat production (mW m^{-3}), C^i is the present-day concentration
358 ([Supplementary Table 8](#)). The average K_2O , Th and U concentrations in the Archean
359 mafic and felsic crust are from Tang et al.⁶¹, and the heat productivity of radioactive
360 element is from Turcotte and Schubert¹⁵. The basic relation between heat flow and
361 geothermal gradient is *Fourier's law*:

$$362 \quad q_B = -k \frac{\Delta T}{\Delta x} \quad (4)$$

363 In this case, the $\frac{\Delta T}{\Delta x}$ represent the geothermal gradient slope ($^{\circ}\text{C km}^{-1}$) of Moho surface.
364 Assuming that the lithospheric mantle does not produce heat ($A = 0 \text{ W m}^{-3}$), we use a
365 MATLAB solution to further constrain the variation trend of Archean continental
366 geotherm. The MATLAB code was attached in the [Supplementary Information](#).

367

368 **Acknowledgements**

369 This research was supported by grants from the National Nature Science Foundation of
370 China (41530207 and 41772188) and Australian Research grant (FL160100168).

371 **Author contributions**

372 S.L. designed the project and developed the initial idea. S.L., G.S., Y.H., and L.G.
373 carried out field geological exploration and sampling. G.S. conducted the experimental
374 analysis and simulations. F.H. compiled the data of Archean TTG gneisses. M.T. and
375 J.v.H. contributed to reconstructing the continental geotherm models. S.L., P.A.C. and
376 G.S. wrote the manuscript. All authors participated in further discussions.

377 **Competing interests**

378 The authors declare no competing interests.

379 **Materials & Correspondence**

380 Correspondence and requests for materials should be addressed to S.L.
381 (swliu@pku.edu.cn) and P.A.C. (peter.cawood@monash.edu).

382 **Additional information**

383 Supplementary information is available in the online version of the paper.

384 **Data availability**

385 The authors declare that all data supporting the findings of this study are available
386 within the article and its Supplementary Information files.

387

388 **References**

- 389 1. Abbott, D., Burgess, L., Longhi, J. & Smith, W. H. F. An empirical thermal history
390 of the Earth's upper mantle. *J. Geophys. Res.* **99**, 13835–13850 (1994).
- 391 2. Kamber, B. The evolving nature of terrestrial crust from the Hadean, through the
392 Archaean, into the Proterozoic. *Precamb. Res.* **258**, 48–82 (2015).
- 393 3. Herzberg, C. Petrological evidence from Komatiites for an early Earth carbon and
394 water cycle. *J. Petrol.* **57**, 2271–2288 (2016).
- 395 4. Putirka, K. Rates and styles of planetary cooling on Earth, Moon, Mars, and Vesta,
396 using new models for oxygen fugacity, ferric–ferrous ratios, olivine–liquid Fe-Mg

- 397 exchange, and mantle potential temperature. *Am. Mineral.* **101**, 819–840 (2016).
- 398 5. van Hunen, J. & van den Berg, A. Plate tectonics on the early Earth: limitations
399 imposed by strength and buoyancy of subducted lithosphere. *Lithos* **103**, 217–235
400 (2008).
- 401 6. Sizova, E., Gerya, T., Brown, M. & Perchuk, L. L. Subduction styles in the
402 Precambrian: insights from numerical experiments. *Lithos* **116**, 209–229 (2010).
- 403 7. Fischer, R. & Gerya, T. Regimes of subduction and lithospheric dynamics in the
404 Precambrian: 3D thermomechanical modelling. *Gondwana Res.* **37**, 53–70 (2016).
- 405 8. Bédard, J. H. A catalytic delamination-driven model for coupled genesis of
406 Archaean crust and sub-continental lithospheric mantle. *Geochim. Cosmochim.*
407 *Acta.* **70**, 1188–1214 (2006).
- 408 9. Dhuime, B., Hawkesworth, C. J., Cawood, P. A. & Storey, C. D. A change in the
409 geodynamic of continental growth 3 billion years ago. *Science* **335**, 1334–1336
410 (2012).
- 411 10. Johnson, T. E., Brown, M., Kaus, B. J. P. & VanTongeren, J. A. Delamination and
412 recycling of Archaean crust caused by gravitational instabilities. *Nat. Geosci.* **7**,
413 47–52 (2013).
- 414 11. Tang, M., Chen, K. & Rudnick, R. L. Archean upper crust transition from mafic to
415 felsic marks the onset of plate tectonics. *Science* **351**, 372–375 (2016).
- 416 12. Cawood, P. A. et al. Geological archive of the onset of plate tectonics. *Philos. Trans.*
417 *A Math. Phys. Eng. Sci.* **376**, 20170405 (2018).
- 418 13. Cawood, P. A. & Hawkesworth, C. J. Continental crustal volume, thickness and

- 419 area, and their geodynamic implications. *Gondwana Res.* **66**, 116–125 (2019).
- 420 14. Davies, G. F. Gravitational depletion of the early Earth's upper mantle and the
421 viability of early plate tectonics. *Earth Planet. Sci. Lett.* **243**, 376–382 (2006).
- 422 15. Turcotte, D. L. & Schubert, G. Geodynamics. Cambridge University Press (2014).
- 423 16. Capitanio, F. A., Nebel, P. A., Cawood, P. A., Weinberg, R. F. & Clos, F.
424 Lithosphere differentiation in the early Earth controls Archean tectonics. *Earth*
425 *Planet. Sci. Lett.* **525**, 115755 (2019).
- 426 17. Chowdhury, P., Chakraborty, S., Gerya, T. V., Cawood, P. A. & Capitanio, F. A.
427 Peel-back controlled lithospheric convergence explains the secular transitions in
428 Archean metamorphism and magmatism. *Earth Planet. Sci. Lett.* **538**, 116224
429 (2020).
- 430 18. Martin, H., Smithies, R. H., Rapp, R., Moyen, J. F. & Champion, D. An overview
431 of adakite, tonalite–trondhjemite–granodiorite (TTG), and sanukitoid:
432 Relationships and some implications for crustal evolution. *Lithos* **79**, 1–24 (2005).
- 433 19. Bai, X., Liu, S. W., Guo, R. R., Zhang, L. F. & Wang, W. Zircon U–Pb–Hf isotopes
434 and geochemistry of Neoproterozoic dioritic–trondhjemitic gneisses, Eastern Hebei,
435 North China Craton: constraints on petrogenesis and tectonic implications.
436 *Precamb. Res.* **251**, 1–20 (2014).
- 437 20. Liou, P. & Guo, J. H. Generation of Archaean TTG Gneisses Through Amphibole-
438 Dominated Fractionation. *J. Geophys. Res.* **124**, 3605–3619 (2019).
- 439 21. Laurent, O. et al. Earth's earliest granitoids are crystal-rich magma reservoirs
440 tapped by silicic eruptions. *Nat. Geosci.* **13**, 1–7 (2020).

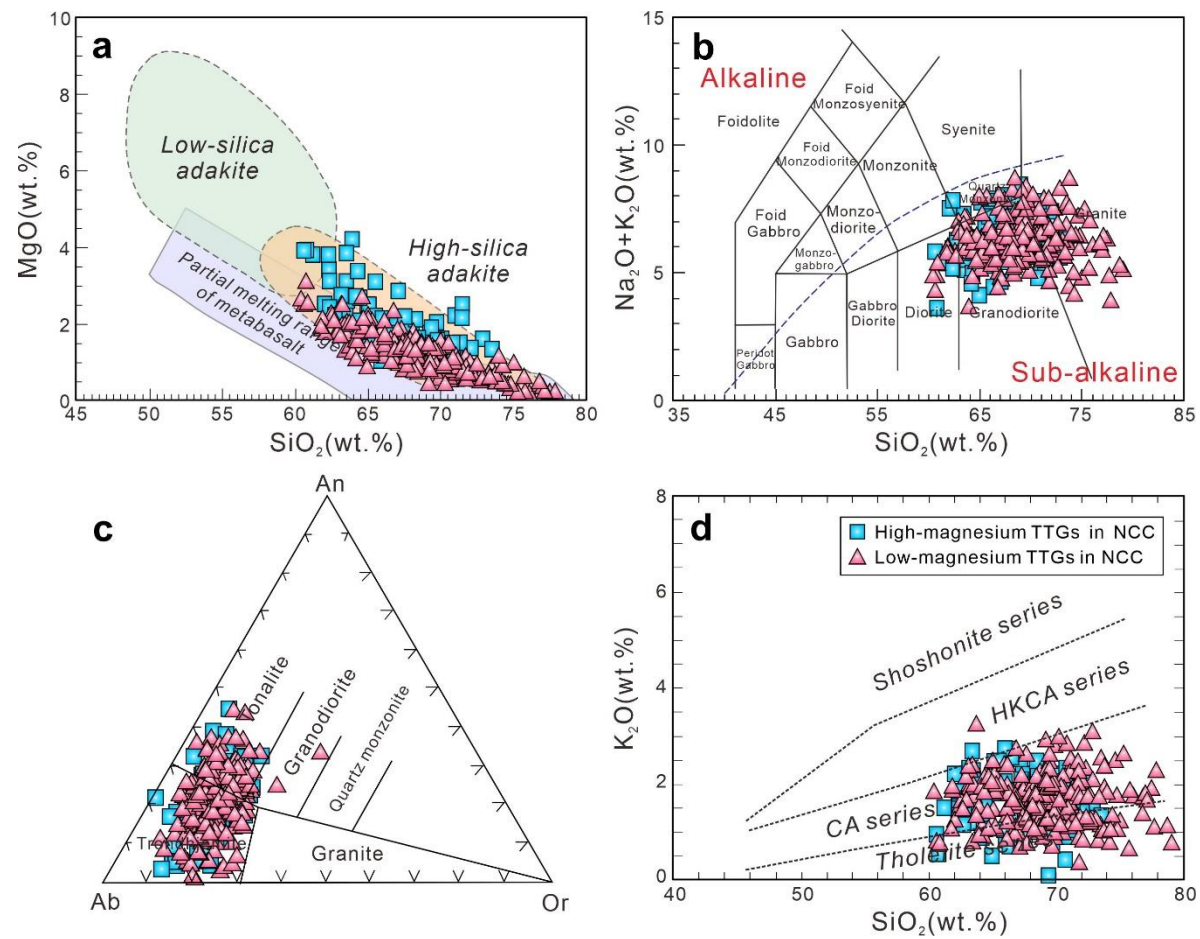
- 441 22. Moyen, J. F. & Martin, H. Forty years of TTG research. *Lithos* **148**, 312–336 (2012).
- 442 23. Sun, G. Z. et al. Thickness and geothermal gradient of Neoproterozoic continental crust:
443 inference from the southeastern North China Craton. *Gondwana Res.* **73**, 16–31
444 (2019).
- 445 24. Drummond, M. S. & Defant, M. J. A model for trondhjemite–tonalite–dacite
446 genesis and crustal growth via slab melting: Archean to modern comparisons. *J.*
447 *Geophys. Res.* **95**, 21503–21521 (1990).
- 448 25. Martin, H. Adakitic magmas: modern analogues of Archean granitoids. *Lithos* **46**,
449 411–429 (1999).
- 450 26. Gao, L. et al. A ca. 2.8 Ga plume-induced intraoceanic arc system in the eastern
451 North China Craton. *Tectonics* **38**, 1694–1717 (2019).
- 452 27. Rapp, R. P. & Watson, E. B. Dehydration melting of metabasalt at 8–32 kbar:
453 implications for continental growth and crust-mantle recycling. *J. Petrol.* **36**, 891–
454 931 (1995).
- 455 28. Rapp, R. P., Shimizu, N., Norman, M. D. & Applegate, G. S. Reaction between
456 slab-derived melts and peridotite in the mantle wedge: experimental constraints at
457 3.8 GPa. *Chem. Geol.* **160**, 335–356 (1999).
- 458 29. Stern, C. R. & Kilian, R. Role of the subducted slab, mantle wedge and continental
459 crust in the generation of adakites from the Andean Austral Volcanic Zone. *Contrib.*
460 *Mineral. Petrol.* **123**, 263–281 (1996).
- 461 30. Chapman, D. S. Thermal gradients in the continental crust. *Acta Anaesthesiologica*
462 *Scandinavica* **24**, 63–70 (1986).

- 463 31. Lee, C. T., Luffi, P. & Chin, E. J. Building and Destroying Continental Mantle.
464 *Annu. Rev. Earth Planet. Sci.* **39**, 59–90 (2011).
- 465 32. Atherton, M. P. & Petford, N. Generation of sodium-rich magmas from newly
466 underplated basaltic crust. *Nature* **362**, 144–146 (1993).
- 467 33. Laurent, O., Martin, H., Moyen, J. F. & Doucelance, R. The diversity and evolution
468 of late-Archean granitoids: evidence for the onset of “modern-style” plate tectonics
469 between 3.0 and 2.5 Ga. *Lithos* **205**, 208–235 (2014).
- 470 34. Ge, R. F., Zhu, W. B., Wilde, S. A. & Wu, H. L. Remnants of Eoarchean continental
471 crust derived from a subducted proto-arc. *Sci. Adv.* **4**, eaao3159 (2018).
- 472 35. Keller, C. B. & Schoene, B. Statistical geochemistry reveals disruption in secular
473 lithospheric evolution about 2.5 Gyr ago. *Nature* **485**, 490–493 (2012).
- 474 36. Polat, A. et al. Geochemical characteristics of the Neoproterozoic (2800–2700 Ma)
475 Taishan greenstone belt, North China craton: evidence for plume–craton interaction.
476 *Chem. Geol.* **230**, 60–87 (2006).
- 477 37. Bao, H., Liu, S. W., Wang, M. J., Teng, G. X. & Sun, G. Z. Mesoarchean
478 geodynamic regime evidenced from diverse granitoid rocks in the Anshan-Benxi
479 area of the North China Craton. *Lithos* **366–367**, 105574 (2020).
- 480 38. Hawkesworth, C. J., Cawood, P. A. & Dhuime, B. Tectonics and crustal evolution.
481 *GSA Today* **26**, 4–11 (2016).
- 482 39. Cawood, P. A. Earth Matters: A tempo to our planet’s evolution. *Geology* **48**, 525–
483 526 (2020).
- 484 40. Wang, W. et al. Neoproterozoic intra-oceanic arc system in the Western Liaoning

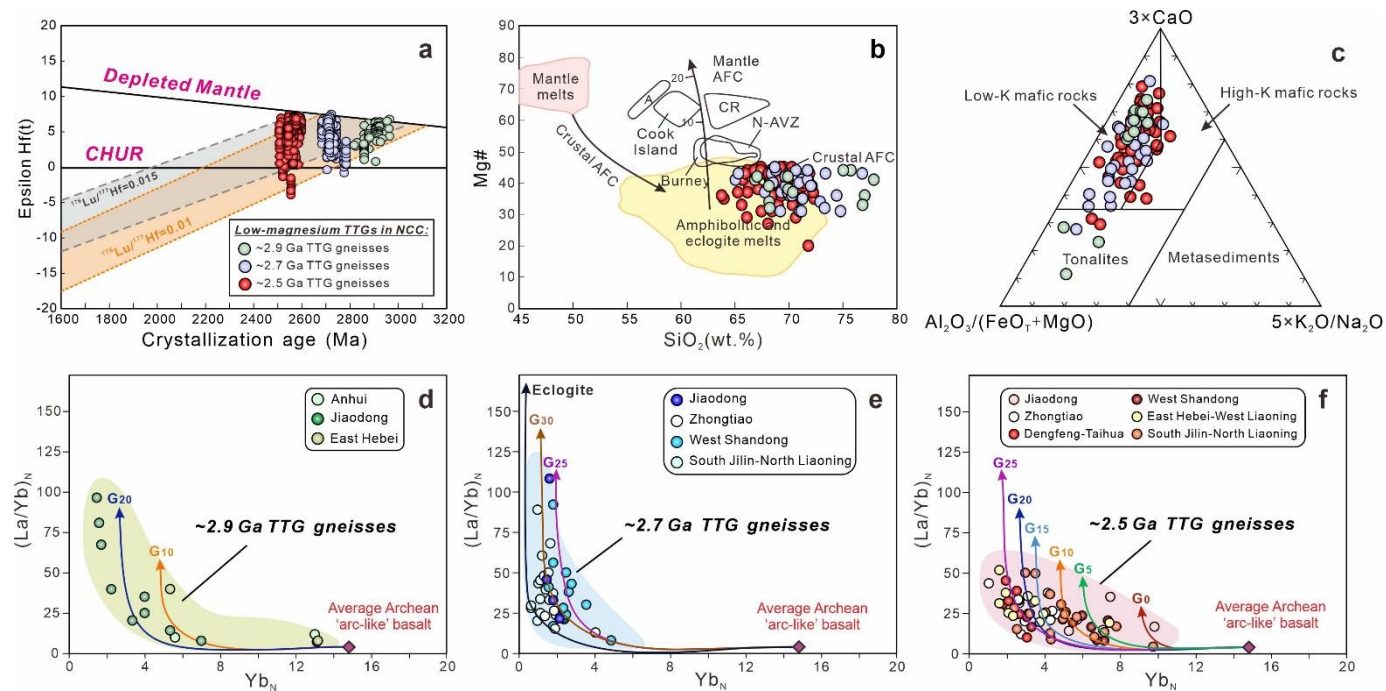
- 485 Province: implications for the Early Precambrian crust-mantle geodynamic
486 evolution of the Eastern Block of the North China Craton. *Earth Sci. Rev.* **150**, 329–
487 364 (2015).
- 488 41. Huang, B. et al. Paired metamorphism in the Neoproterozoic: A record of accretionary-
489 to-collisional orogenesis in the North China Craton. *Earth Planet. Sci. Lett.* **543**,
490 116355 (2020).
- 491 42. Currie, C. A. & Hyndman, R. D. The thermal structure of subduction zone back
492 arcs. *J. Geophys. Res.* **111**, 1–22 (2006).
- 493 43. Liu, S. W. et al. Precambrian geodynamics (VII): formation and evolution of early
494 continental crust. *Earth Sci. Front.* **22**, 97–108 (2015) (in Chinese with English
495 abstract).
- 496 44. Fu, J. H., Liu, S. W., Zhang, B., Guo, R. R. & Wang, M. J. A Neoproterozoic K-rich
497 granitoid belt in the northern North China Craton. *Precamb. Res.* **328**, 193–216
498 (2019).
- 499 45. Zhang, J., Zhang, H. F., Li, L. & Wang, J. L. Neoproterozoic-Paleoproterozoic tectonic
500 evolution of the southern margin of the North China Craton: Insights from
501 geochemical and zircon U–Pb–Hf–O isotopic study of metavolcanic rocks in the
502 Dengfeng complex. *Precambrian Res.* **318**, 103–121 (2018).
- 503 46. Wan, Y. S. et al. Zircon ages and geochemistry of late Neoproterozoic syenogranites in
504 the North China Craton: a review. *Precambrian Res.* **222–223**, 265–289 (2012).
- 505 47. Heilimo, E., Halla, J. & Hölttä, P. Discrimination and origin of the sanukitoid series:
506 geochemical constraints from the Neoproterozoic western Karelian Province (Finland).

- 507 *Lithos* **115**, 27–39 (2010).
- 508 48. Sun, G. Z., Liu, S. W., Wang, M. J., Bao, H. & Teng, G. X. Complex Neoproterozoic
509 mantle metasomatism: Evidence from sanukitoid diorites-monzodiorites-
510 granodiorites in the northeastern North China Craton. *Precambrian Res.* **342**,
511 105692 (2020).
- 512 49. Moyen, J. F. The composite Archaean grey gneisses: petrological significance, and
513 evidence for a non-unique tectonic setting for Archaean crustal growth. *Lithos* **123**,
514 21–36 (2011).
- 515 50. McLennan, S. M. Earth's Continental Crust. Springer Netherlands (1998).
- 516 51. Dhuime, B., Wuestefeld, A. & Hawkesworth, C. J. Emergence of modern
517 continental crust about 3 billion years ago. *Nat. Geosci.* **8**, 552–555 (2015).
- 518 52. Robin, C. M. I. & Bailey, R. C. Simultaneous generation of Archean crust and
519 subcratonic roots by vertical tectonics. *Geology* **37**, 523–526 (2009).
- 520 53. Rapp, R. P., Shimizu, N. & Norman, M. D. Growth of early continental crust by
521 partial melting of eclogite. *Nature* **425**, 605–609 (2003).
- 522 54. Wyllie, P. J. & Wolf, M. B. Amphibole dehydration-melting: Sorting out the solidus.
523 In: Pritchard, H.M., Alabaster, T., Harris, N.B.W., Neary, C.R. (eds.). Magmatic
524 Processes and Plate Tectonics. *Geol. Soc., London Spec. Publ.* **76**, 405–416 (1993).
- 525 55. Holland, T. J. B. & Powell, R. An internally consistent thermodynamic data set for
526 phases of petrological interest. *J. Metamorph. Geol.* **16**, 309–344 (1998).
- 527 56. Green, E. C. R. et al. Activity-composition relations for the calculation of partial
528 melting equilibria in metabasic rocks. *J. Metamorph. Geol.* **34**, 845–869 (2016).

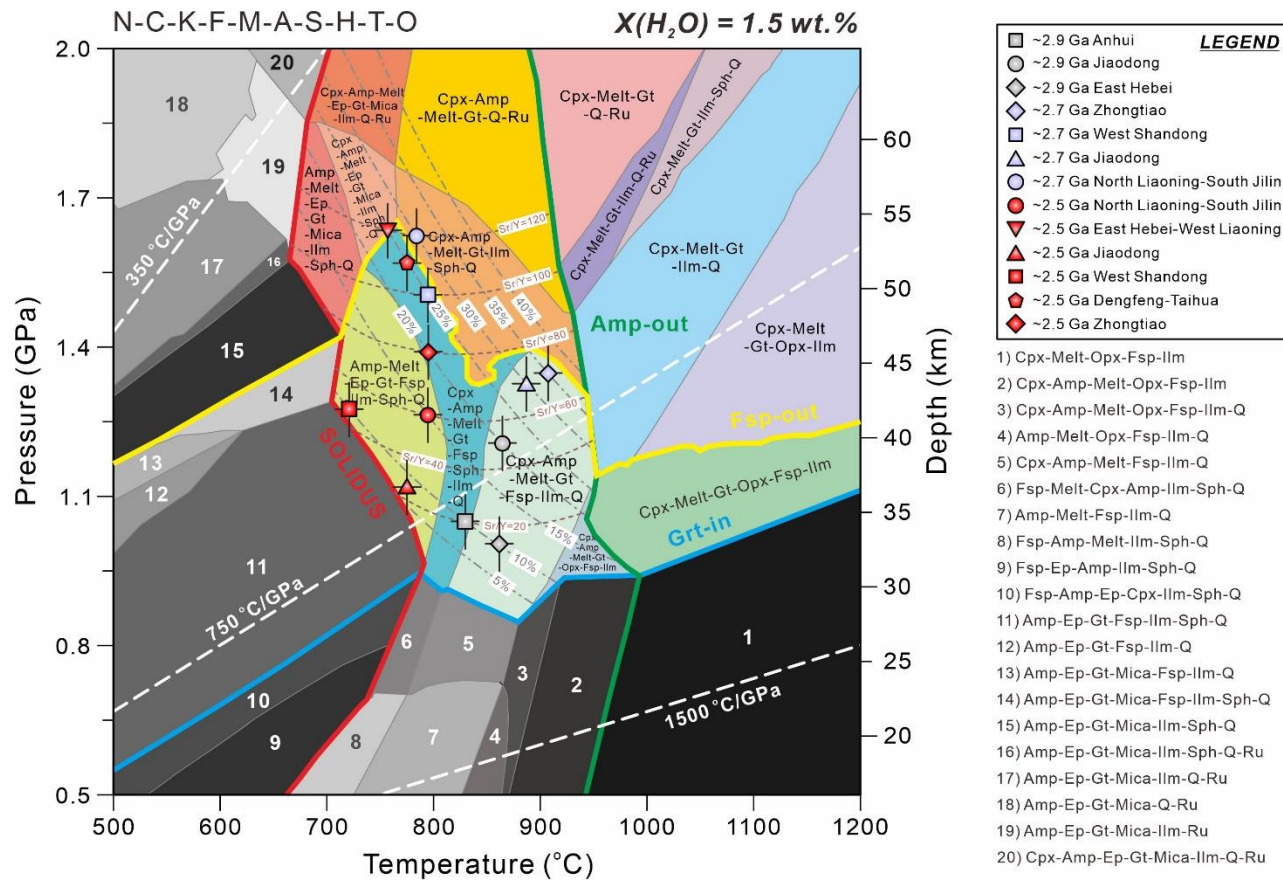
- 529 57. White, R. W., Powell, R. & Johnson, T. E. The effect of Mn on mineral stability in
530 metapelites revisited: New a–x relations for manganese-bearing minerals. *J.*
531 *Metamorph. Geol.* **32**, 809–828 (2014).
- 532 58. Holland, T. J. B. & Powell, R. Activity–composition relations for phases in
533 petrological calculations: An asymmetric multicomponent formulation. *Contrib.*
534 *Mineral. Petrol.* **145**, 492–501 (2003).
- 535 59. Holland, T. J. B. & Powell, R. An improved and extended internally consistent
536 thermodynamic dataset for phases of petrological interest, involving a new
537 equation of state for solids. *J. Metamorph. Geol.* **29**, 333–383 (2011).
- 538 60. Shaw, D. M. Trace element fractionation during anatexis. *Geochim. Cosmochim.*
539 *Ac.* **34**, 237–243 (1970).
- 540 61. Tang, M., Lee, C. T., Rudnick, R. L. & Condie, K. C. Rapid mantle convection
541 drove massive crustal thickening in the late Archean. *Geochim. Cosmochim. Ac.*
542 **278**, 6–15 (2020).
- 543 62. Middlemost, E. A. K. Naming materials in the magma/igneous rock system. *Annu.*
544 *Rev. Earth Pl. Sc.* **37**, 215–224 (1994).
- 545 63. Barker, F. Trondhjemite: definition, environment and hypotheses of origin, in
546 Barker, F., editor, Trondhjemites, Dacites and Related Rocks: Amsterdam, Elsevier,
547 p. 1–12 (1979).
- 548 64. Rollinson, H. Using Geochemical Data: Evaluation, Presentation, Interpretation.
549 Longman Scientific and Technical, London, pp. 52–61 (1993).



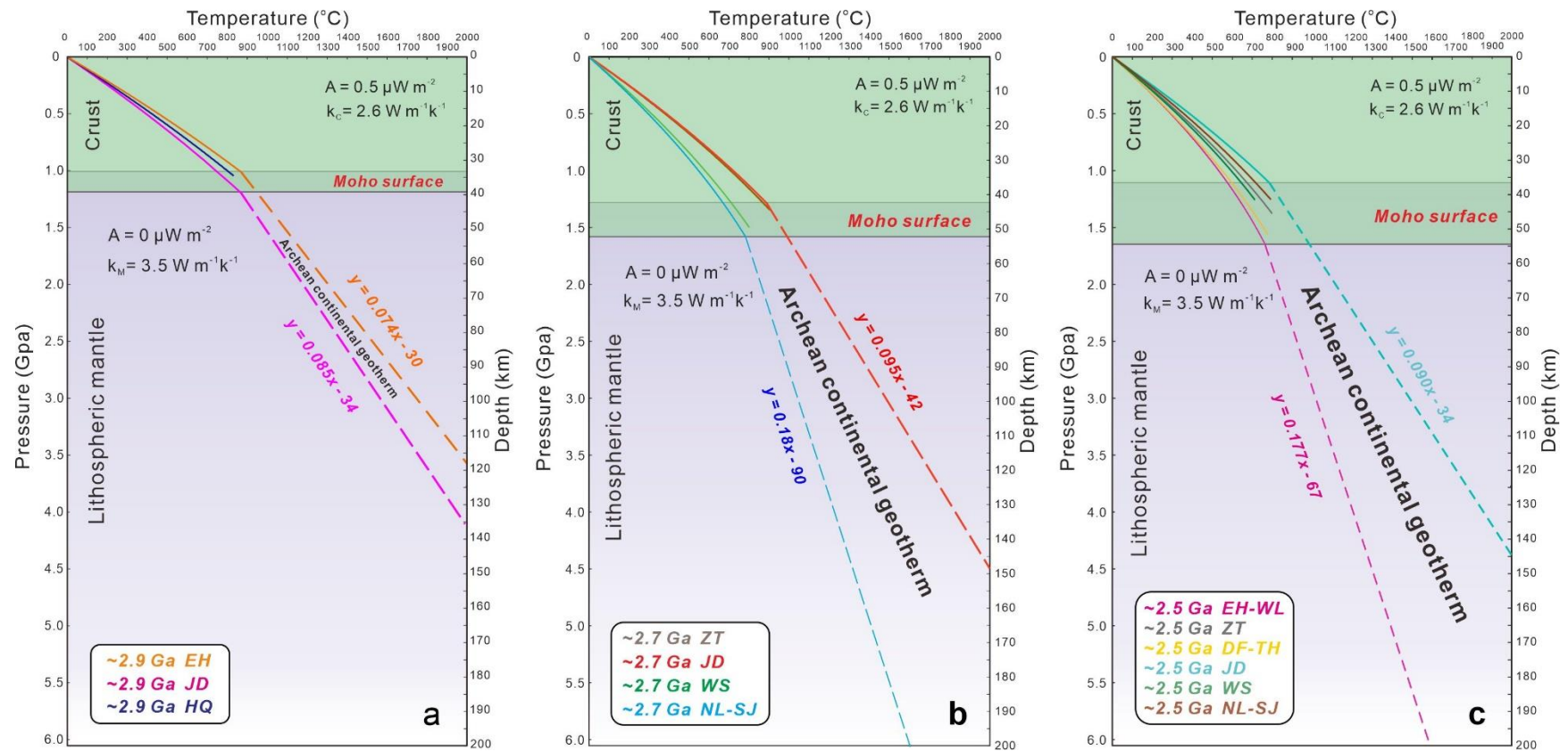
550 **Fig. 1** Geochemical diagrams for the Meso- to Neoproterozoic TTG gneisses from the Eastern Block of the NCC. **a** MgO versus SiO₂ diagram (after Martin et
 551 al.¹⁸); **b** Total alkalis versus silica diagram (TAS, after Middlemost⁶²); **c** An-Ab-Or diagram (after Barker⁶³); **d** K₂O versus SiO₂ classification diagram (after
 552 Rollinson⁶⁴).



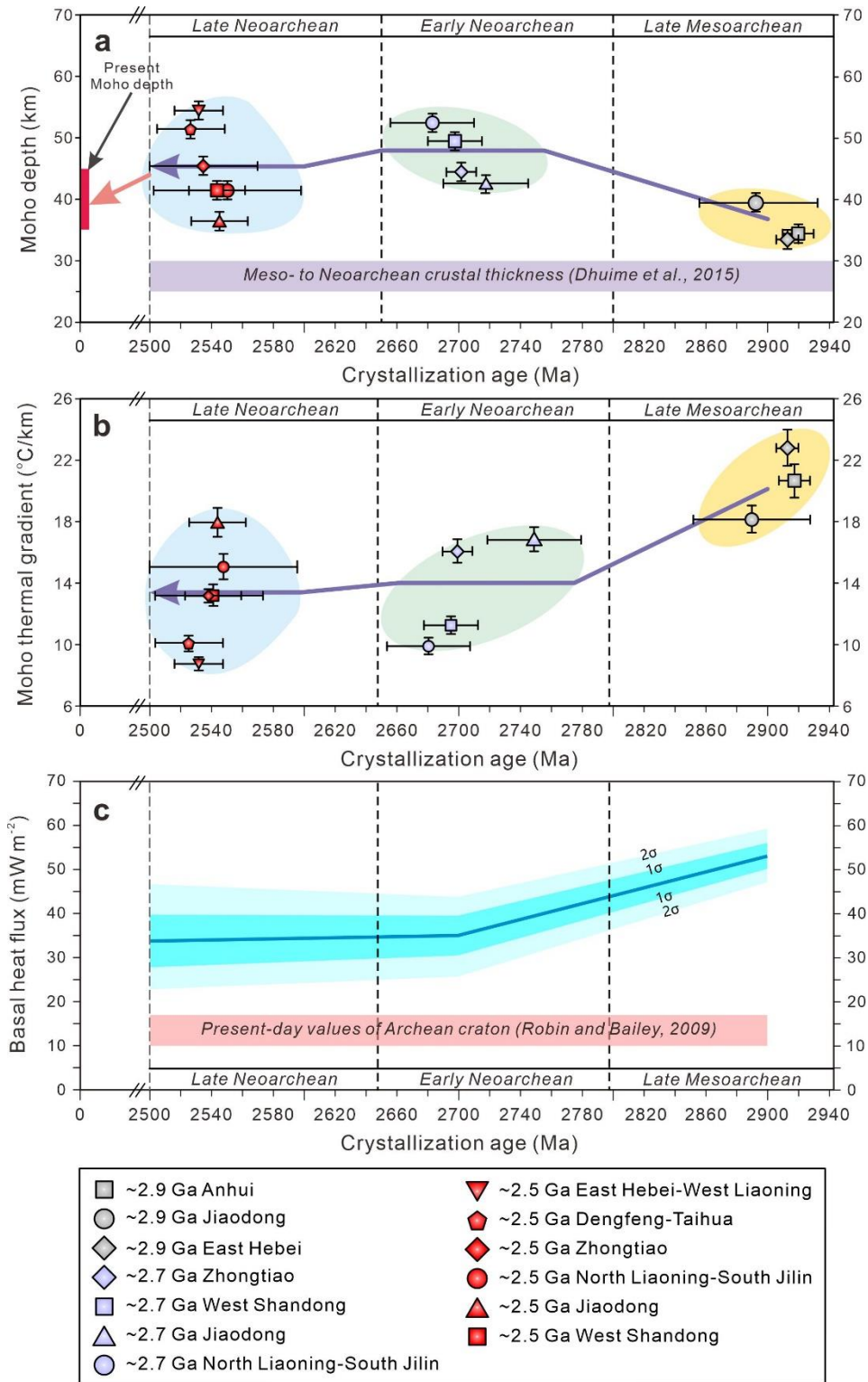
553 **Fig. 2** Petrogenetic identification diagrams of TTG gneisses. **a** Plots of the zircon $\epsilon\text{Hf}(t)$ values versus crystallization ages (Ma) for the dated TTG gneiss
 554 samples in the Eastern Block of the NCC; **b** Mg# versus SiO_2 diagram (modified after Stern and Killian²⁹). This also shows the field for pure crustal partial
 555 melts obtained in experimental studies by dehydration melting of amphibolitic rocks and eclogites^{27,28}; **c** Ternary diagram of $\text{Al}_2\text{O}_3/(\text{FeO}_T + \text{MgO})$, $3 \times \text{CaO}$,
 556 and $5 \times (\text{K}_2\text{O}/\text{Na}_2\text{O})$. The fields represent the composition of melts derived from a range of potential sources of tonalites, metasediments, and low- and high-K
 557 mafic rocks³³; **d-f** $(\text{La}/\text{Yb})_N$ versus Yb_N diagrams. The color curve in the inset represents batch partial melting trends with different residual mineral
 558 assemblages. The source in the inset is an average Archean ‘arc-like’ basalt transformed into 0% (G_0), 5% (G_5), 10% (G_{10}), 15% (G_{15}), 20% (G_{20}), 25% (G_{25})
 559 and 30% (G_{30}) garnet-bearing amphibolite (after Moyen⁴⁹).



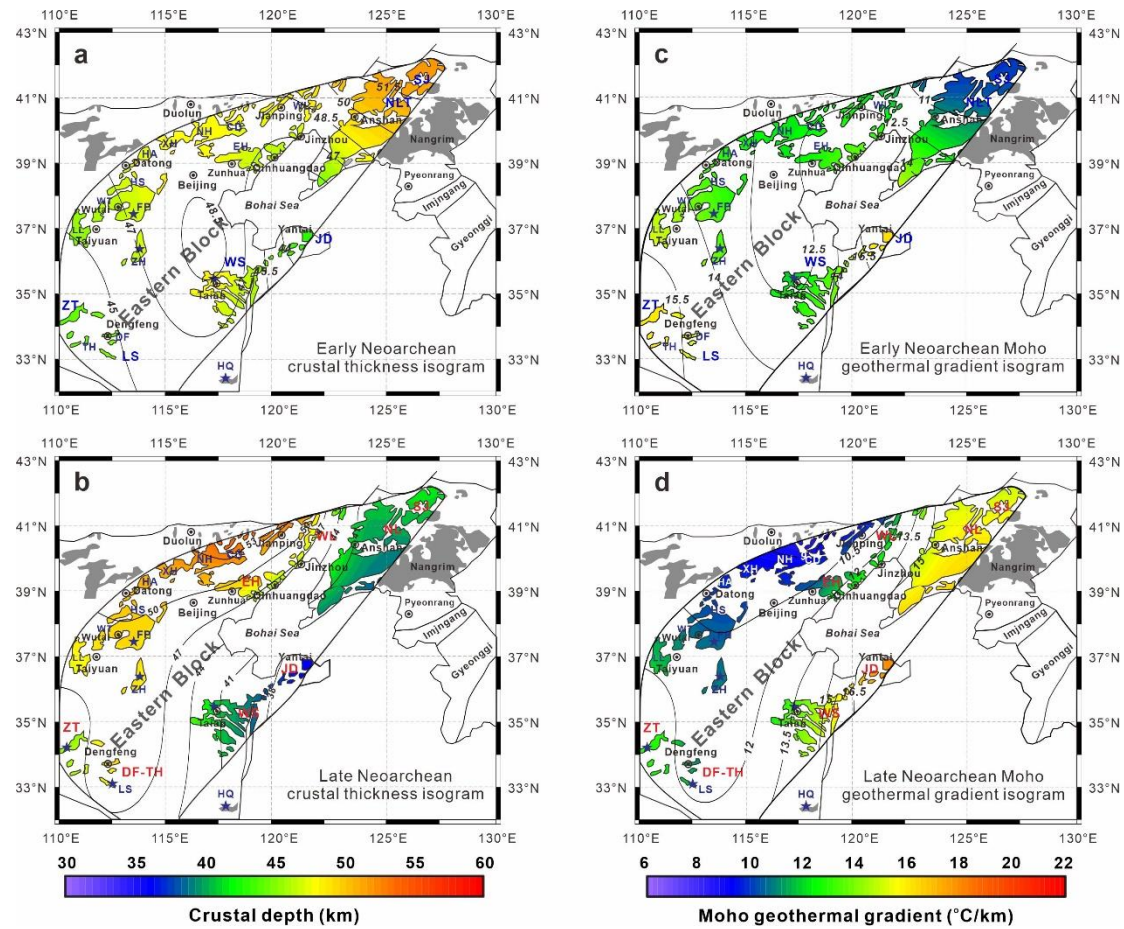
560 **Fig. 3** Thermodynamic and trace element modelling. Simplified P–T phase diagram for the median composition of Archean ‘arc-like’ basalts ([Supplementary](#)
 561 [Table 7](#)), calculated with $X(H_2O) = 1.5 \text{ wt.}\%$, corresponding to dehydration melting of metamorphosed basalt. Long and short dashed lines represent the
 562 garnet proportion (%) in residue and melt Sr/Y ratios, respectively; solid lines show major phase boundaries: red–melt (solidus), blue–garnet, green–
 563 amphibole, and yellow–feldspar. Error bars are 1σ based on uncertainties of observed garnet proportion (%) and Sr/Y ratios.



564 **Fig. 4** Generic model for the Meso- to Neoproterozoic thermal evolution of the NCC. In this model, the Archean continental geotherm was constrained assuming
 565 a steady-state conductive geotherm, without considering the effects of heat convection of the asthenosphere mantle. The depth of Moho surface is determined
 566 by melting pressure of crustal-derived TTG melts, whereas the Archean lithospheric thickness is uncertain.



567 **Fig. 5** Changes of calculated crustal thickness (a), Moho geothermal gradient (b) and basal
 568 heat flux (c) over time for the Eastern Block of the NCC. The present Moho depth is from
 569 McLennan⁵⁰, and the conventional wisdom about Meso- to Neoproterozoic crustal thickness is
 570 from Dhuime et al.⁵¹. The present-day basal heat flux values of Archean craton are from
 571 Robin and Bailey⁵².



572 **Fig. 6** Contour color plots of crustal thickness and Moho geothermal gradient in the Eastern Block of the NCC at different periods. **a** and **c** early Neoproterozoic
 573 (~2.7 Ga); **b** and **d** late Neoproterozoic (~2.5 Ga). Abbreviations for the metamorphic basements: SJ—South Jilin; NL—North Liaoning; SL—South Liaoning;
 574 EH—East Hebei; WL—West Liaoning; JD—Jiaodong; WS—West Shandong; DF-TH—Dengfeng-Taihua; ZT—Zhongtiao.